Interferometric Hartmann wave-front sensing for active optics at the 6.5-m conversion of the Multiple Mirror Telescope

Steven C. West

A little-used interferometric modification to the classical Hartmann optical test is being used for active optics corrections at the 6.5-m Multiple Mirror Telescope (MMT) Observatory. The technique produces compact interference spots whose positions depend on discrete wave-front phase-difference errors. A diffraction model illustrates the formation of interference spots. The limitations on wave-front sampling that are due to atmospheric seeing are estimated. Two data reduction matrix strategies are given. A single correction of collimation and primary mirror figure produces a nearly diffraction-limited telescope image. Wave-front polynomial coefficients ranging from several nanometers to several micrometers in amplitude are reliably detected.

OCIS codes: 050.1220, 050.1940, 050.5080, 120.1680, 350.1260, 120.3180.

1. Introduction

It has been more than 15 years since Korhonen described the development and use of an interferometric modification to the classical Hartmann optical test.[1–4] In this device, which should perhaps be called the Korhonen–Hartmann wave-front sensor, a Hartmann aperture array and a single converging camera lens replace the familiar lenslet array of the Shack–Hartmann. In regions away from the camera lens focus, an array of Young's-type interference spots are formed by the overlapping Hartmann aperture beams. Variations in the spot grid spacing are proportional to the phase differences in the apertures. Because each spot is formed by interference, it is much smaller than the corresponding diffraction spot image produced by a lenslet that is the same diameter as the Hartmann aperture. Smaller spots provide potential advantages both in terms of efficient detector usage and better detection of small wave-front errors because the spot displacement is a larger fraction of the spot diameter.

There are several disadvantages to the interferometric Hartmann. Unlike the Shack–Hartmann, the dynamic range is limited because the spot motion is cyclic in multiples of the wavelength. Compared with techniques such as curvature sensing, shearing, or Shack-cube interferometry, for example, this technique suffers from coarse pupil sampling. This disadvantage is exacerbated because, the smaller the desired interference spots, the coarser the wave-front sampling required. Changing the wave-front sampling within the beam requires a refocusing of the detector.

Although only briefly mentioned here, use of this technique to measure step-phase errors remains largely unexplored. This contrasts to the powerful and well-developed technique used to phase the primary mirror segments of the Keck telescopes. The Keck technique exploits diffraction effects within a single subaperture overlapping the boundary between two segments. When the relatively complex broadband diffraction image is correlated with 11 coherent image templates (spanning phase differences from 0 to 2π), the degree of coherence between the segments is determined. This technique is capable of detecting piston errors as large as 30 μm and reducing them to 30 nm.[5] More recently, a monochromatic refinement improves the phasing accuracy to 6 nm.[6] In contrast, an interferometric Hartmann solution would exploit the phase difference between pairs of apertures located on opposite sides of the boundary between segments. The phasing errors would be determined by measurement of the displacement of the interferometric spots from the reference positions. Removing multiple-wavelength ambiguities from phasing errors would require careful thought and analysis. It is beyond the scope of

S. C. West (swest@as.arizona.edu) is with the Multiple Mirror Telescope Observatory, University of Arizona, Tucson, Arizona 85721-0065.

Received 4 October 2001; revised manuscript received 14 February 2002.

0003-6935/02/193781-09$15.00/0

this paper to investigate the interferometric Hartmann in applications where multiple-wavelength ambiguities occur.

Given the recent explosion of wave-front analysis in the fields of microscopy, astronomy, and precision metrology, the Korhonen–Hartmann technique deserves consideration in applications requiring high-precision wave-front measurements.

In this paper I present a review of the interferometric Hartmann optical test and then summarize the first active optics results at the 6.5-m Multiple Mirror Telescope (MMT, although MM has no current meaning aside from tradition) $f/9$ focus. The telescope and active optics system is described in Section 2. In Section 3, the basic equations describing aperture beam interference are reviewed, the limitations of use because of atmospheric turbulence are estimated, and the results of simple diffraction models that illustrate the formation of interference spots and the detection of phase differences are presented. Two matrix strategies for phase reconstruction and for the fitting of wave-front gradient polynomials are shown in Section 4. The instrument and software design are briefly summarized in Section 5. Finally, in Section 6 I present the first results for collimation and mirror figure correction using the interferometric Hartmann wave-front analyzer at the 6.5-m MMT $f/9$ focus.

2. Conversion of the 6.5-m Multiple Mirror Telescope to a 6.5-m Aperture

After 21 years of service, the six 1.8-m primary mirrors of the MMT were replaced with a single 6.5-m $f/1.25$ honeycomb borosilicate primary mirror manufactured at the Steward Observatory Mirror Laboratory.[7] The building and original azimuth drive system were modified to accept a new optical support structure, and in May 2000 the $f/9$ Hextek secondary mirror was installed.[8–10] The new facility is called the 6.5-m MMT Observatory. In the near future, two new secondaries will be added—a wide-field $f/5.2$ and an adaptive $f/15$.[11–13]

The active optics system consists of 104 primary mirror axial actuators and a six-degree-of-freedom hexapod secondary positioner.[14–18] Both the $f/9$ and $f/5.2$ secondary mirror support systems do not incorporate active figure control. Any figure error they have is corrected with the primary mirror.

The interferometric Hartmann wave-front sensor is primarily intended for stand-alone active optics studies at the $f/9$ and $f/5$ Cassegrain foci including the development of elevation-dependent look-up tables to correct the effects of gravity on the mirror figure and collimation, localized mirror support errors, and low-frequency thermal control errors in the honeycomb borosilicate ventilation system.

3. Brief Overview of the Interferometric Hartmann Technique

The interferometric Hartmann analyzer directly measures discrete phase differences in the wave front in contrast to the Shack–Hartmann analyzer that directly measures discrete wave-front gradients. Instead of using a lenslet array, the interferometric device uses a simple Hartmann aperture array placed, for example, at the collimated image of the entrance pupil. A single converging camera lens (placed behind the aperture mask) focuses the Airy patterns produced by the individual apertures (Fig. 1). Although use of a reimaged pupil has advantages in some applications, one need only place the Hartmann mask in a converging optical beam away from the image caustic.

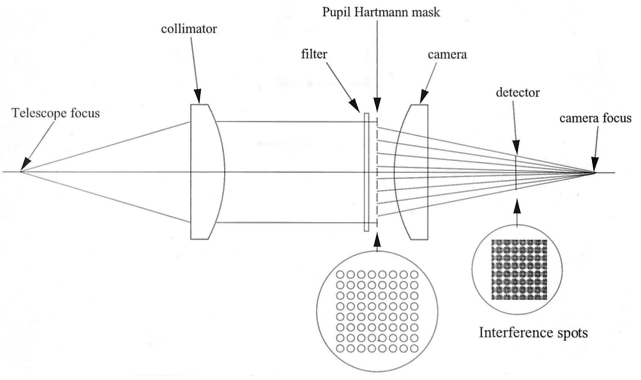

Fig. 1. Typical interferometric Hartmann optical path that utilizes a reimaged pupil for use at a telescope. The Hartmann mask is placed at the image of the collimated pupil. An array of $m = 0$ interference spots is created on the detector away from the camera focus.

The relatively large Airy disks created by the Hartmann apertures overlap and interfere with one another in the beam of the camera lens. Looking more closely at the pattern of spots on the detector, we find that groups of four apertures (a quartet) produce sharp $m = 0$ interference in these overlapping regions. The exact positions of the interference spots depend on the phase differences between apertures as depicted by one quartet in Fig. 2.

Using the familiar two-slit formula to solve for the position of the maximum on a detector, but noting

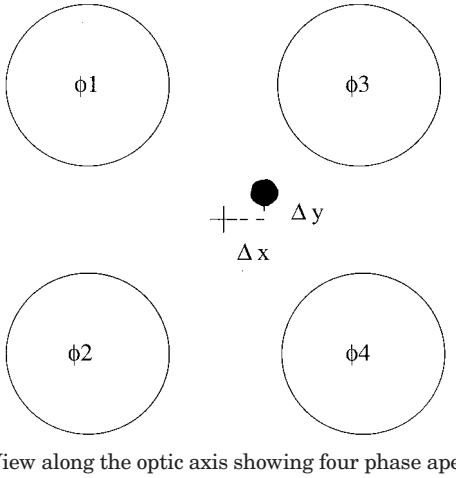

Fig. 2. View along the optic axis showing four phase apertures in the pupil plane and the interference spot they form on the detector. The shift $(\Delta x, \Delta y)$ of the spot from the center depends on the phase differences within the apertures.

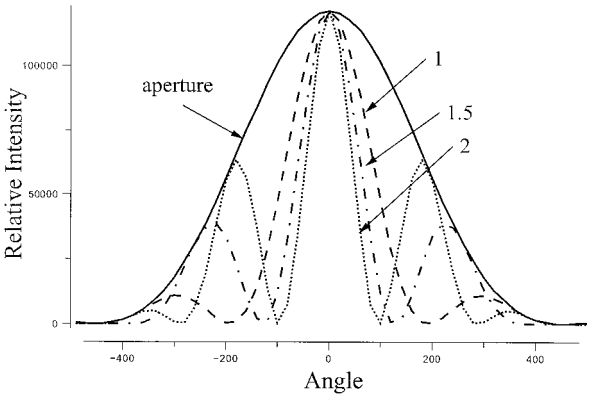

Fig. 3. One-dimensional monochromatic diffraction at the camera focus formed by two Hartmann apertures (with identical phases) for several ratios of aperture spacing to diameter D/d. This illustrates how geometry can be used to isolate the $m = 0$ fringe. The figure is drawn for constant aperture size d for simplicity.

that we have four phase apertures, we can relate the aperture phase differences to the image centroid position errors Δx and Δy by

$$\Delta\phi x = (\phi_3 + \phi_4) - (\phi_1 + \phi_2) = \frac{2D\Delta x}{f}, \qquad (1)$$

$$\Delta\phi y = (\phi_1 + \phi_3) - (\phi_2 + \phi_4) = \frac{2D\Delta y}{f}, \qquad (2)$$

where D is the aperture spacing and f is the camera focal length. Korhonen notes that Eqs. (1) and (2) are simplified if the coordinate system is rotated by 45 deg.[1]

A. Interference at the Camera Focus

A brief look at two-aperture diffraction at the camera focus serves to illustrate a few points about the interferometric Hartmann technique. In Fig. 3 we can see the Young's two-slit diffraction modulated within the sinc^2 envelope of a single aperture. The size of the diffraction from a single aperture (or an equivalent Shack–Hartmann lenslet) is inversely proportional to its diameter ($2.44\lambda/d$), where λ is the wavelength of light. The corresponding minimum-to-minimum width of the interference is inversely proportional to the aperture spacing (λ/D). All else being equal, the interference spots can therefore be made significantly smaller ($2.44D/d$) than the corresponding spot from a lenslet or classical Hartmann test. We obtain better detection of small wave-front errors because the spot motion is now a larger fraction of the spot diameter. The smaller spot size also improves the instrument designer's ability to pack more pupil sampling onto a given detector format.

The geometry can be used to isolate the $m = 0$ interference because the aperture diameter controls the sinc^2 envelope width. Clearly, $D/d = 1$ provides the best suppression of high-order interference and the largest light throughput. Decreasing the aperture diameter d broadens the aperture diffraction envelope making the device robust to large tilt variations between apertures at the expense of admitting higher-order interference. However, the unwanted effects of higher-order interference are mitigated when the optical bandpass is enlarged. The $m = 0$ interference overlaps independent of color, but the higher-order fringes smear out into spectra, diminishing their unwanted effects. For the research reported here, $D/d \sim 1.5$, but Korhonen has used ratios >3 effectively.

Larger aperture spacing D produces narrower interference and hence better phase error detection for the reason stated above. Compared with optical testing in a thermally controlled laboratory environment, atmospheric seeing limits the attainable aperture spacing at the telescope. For Kolmogorov turbulence, the root-mean-square phase difference that is due to the atmosphere ($\delta\phi$) depends on the spatial separation of the sampling x within the entrance pupil[19,20]:

$$\delta\phi(\text{waves}) = 0.4175\left(\frac{x}{r_0}\right)^{5/6}. \qquad (3)$$

The coherence diameter r_0 is the separation corresponding to a phase error of 0.4175 waves at the wavelength of interest. It is related to the long-exposure atmospheric seeing full width at half-maximum image size θ by

$$\theta(\text{arc sec}) \simeq 20.2\,\frac{\lambda}{r_0}, \qquad (4)$$

where r_0 and λ are measured in centimeters and micrometers, respectively.

An upper limit for D as a function of seeing can be estimated when we set the rms phase variation $\delta\phi \sim 1/2$ wave. Solving for the spacing x, we find that, in the presence of 1-arc sec seeing, the aperture spacing must be less than 200 mm for $\lambda = 0.8\ \mu\text{m}$. Matching the seeing to the angular spacing of the interference ($\theta \sim \lambda/D$) confirms the magnitude of this limit.

B. Interference Away from the Camera Focus

As more apertures are added in one dimension, the interference fringes at the camera focus simply narrow in a manner analogous to the addition of more rulings to a diffraction grating. To resolve the phase-difference distribution over the extent of the pupil, the detector must be shifted away from the camera focus so that individual $m = 0$ fringes are spatially separated on the detector. The detector is placed at the position in the beam where a given $m = 0$ fringe overlaps the $m = \pm 1$ fringe from the adjacent interference pattern[1]:

$$ds = \lambda\left(\frac{f}{D}\right)^2, \qquad (5)$$

where λ is the wavelength of light, f is the camera focal length, and D is the aperture spacing.

Prior to constructing an instrument, we investigated the interference geometry with a diffraction

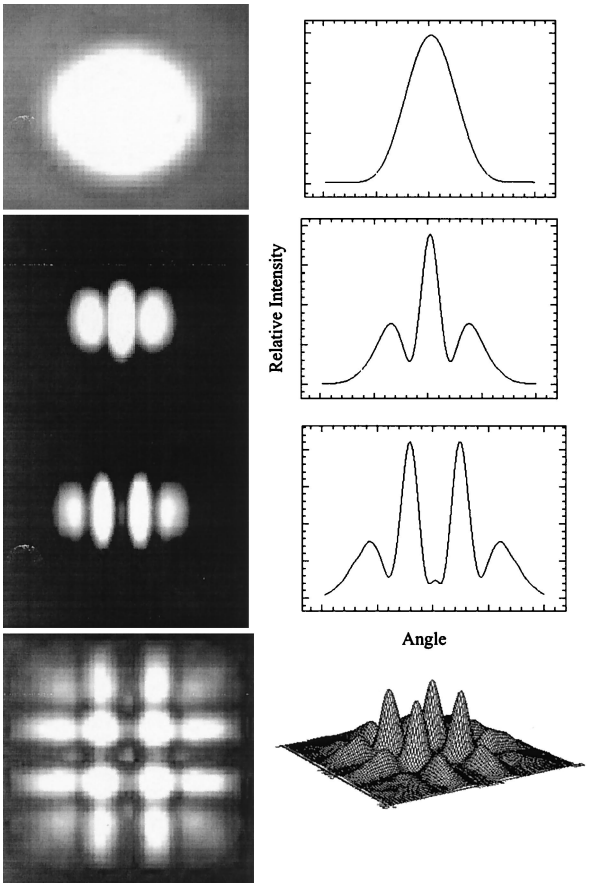

Fig. 4. Two-dimensional interference model for $D/d = 1.5$ illustrates how compact interference spots are formed at the detector position given by Eq. (5). Shown is a series of images (left column all to same scale) and corresponding intensity distributions (right column). A single defocused Hartmann Airy disk is shown at the top. The next two images show interference from a row of two and three Hartmann apertures. The bottom image illustrates the four $m = 0$ interference spots that are produced by a 3×3 grid of Hartmann apertures.

modeling program. A C algorithm was developed to sum a phase distribution from discrete apertures on a spherical wave front into a detector pixel array with a provision for shifting the detector an arbitrary distance from the camera focus. The calculation is performed for monochromatic light or for a range of wavelengths in a bandpass. This program provides a useful way to investigate the formation of interference as a function of detector position and aperture geometry. Figure 4 shows the defocused Airy disk from one Hartmann aperture and then the interference from two and three apertures in a line. Finally, the formation of four compact $m = 0$ spots created by a 3×3 aperture grid is shown. All images are displayed at the same scale. Beside each image is the relative intensity plot. The position of the detector is given by Eq. (5).

Figure 5 shows a one-dimensional model of diffraction created with a line of five apertures. The detector is shifted away from the camera focus by the amount in Eq. (5). Each pair of apertures produces

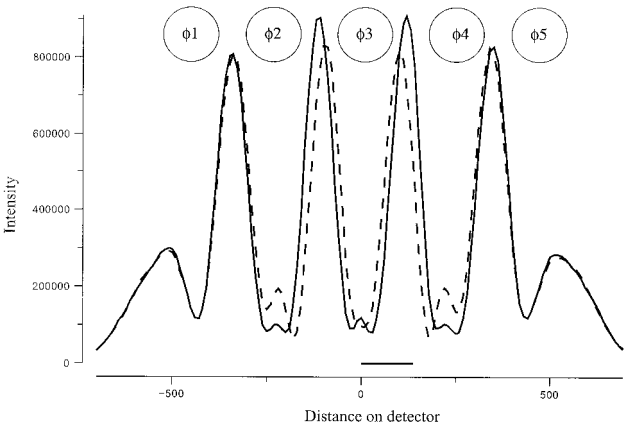

Fig. 5. One-dimensional model of the interference created by five Hartmann apertures in a row. The detector is shifted away from the camera focus by the amount given in Eq. (5). Four well-defined interference spots are shown with all five phases equal (solid curve) and for ϕ_3 shifted in piston by $+1/8$ wave (dashed curve).

a distinct $m = 0$ interference spot. A $+1/8$ wave piston phase shift in aperture three causes the two nearest interference spots to shift (as shown by the dashed curve).

4. Determining the Wave-Front Error

Whether a Shack– or Korhonen–Hartmann analyzer is employed, the same basic data reduction is required. The instrumental wave-front errors are subtracted from the wave front sampled in the telescope beam. The resulting wave-front error distribution is fitted to a set of polynomials or used to reconstruct raw phases. The wave-front errors are used to tune optical collimation and optimize the primary mirror figure.

A. Gradient Solution

We start with M sampling points within the pupil. For each point i, centered on a dimensionless pupil coordinate (x_i, y_i), we observe the total x and y wave-front gradients $(\partial W_i/\partial x, \partial W_i/\partial y)$ by measuring the image displacement of the $m = 0$ interference spot. The gradient information is obtained directly from the Shack–Hartmann, but must be computed from the phase differences with the interferometric device:

$$\frac{\partial W_i}{\partial x} = \frac{\Delta\phi x_i}{2ap\ sp}, \tag{6}$$

$$\frac{\partial W_i}{\partial y} = \frac{\Delta\phi y_i}{2ap\ sp}, \tag{7}$$

where $\Delta\phi x_i$ and $\Delta\phi y_i$ are given by Eqs. (1) and (2), respectively, and ap sp is the Hartmann aperture spacing projected onto the dimensionless pupil.

The wave front W_i at a given point i is described by N polynomials Z_j with amplitude coefficients C_j by

$$W(x_i, y_i) = \sum_{i=1}^{N} Z_j(x_i, y_i) C_j = W_i. \tag{8}$$

The matrix describing the relationship of the discrete wave-front errors seen on the detector to the polynomial gradients is

$$\begin{bmatrix} \frac{\partial Z_1}{\partial x}(x_1, y_1) & \cdots & \frac{\partial Z_N}{\partial x}(x_1, y_1) \\ \vdots & \vdots & \vdots \\ \frac{\partial Z_1}{\partial x}(x_M, y_M) & \cdots & \frac{\partial Z_N}{\partial x}(x_M, y_M) \\ \frac{\partial Z_1}{\partial y}(x_1, y_1) & \cdots & \frac{\partial Z_N}{\partial y}(x_1, y_1) \\ \vdots & \vdots & \vdots \\ \frac{\partial Z_1}{\partial y}(x_M, y_M) & \cdots & \frac{\partial Z_N}{\partial y}(x_M, y_M) \end{bmatrix} \begin{bmatrix} C_1 \\ \vdots \\ C_N \end{bmatrix} = \begin{bmatrix} \frac{\partial W_1}{\partial x} \\ \vdots \\ \frac{\partial W_M}{\partial x} \\ \frac{\partial W_1}{\partial y} \\ \vdots \\ \frac{\partial W_M}{\partial y} \end{bmatrix}. \tag{9}$$

The columns of the matrix describe the influence of each wave-front gradient polynomial on the total wave-front gradient measured on the detector. Equation (9) has the form $[A](x) = (b)$, where $[A]$ is a $2M \times N$ matrix. We solve for the polynomial coefficients (x) using singular value decomposition.

B. Phase Solution

One method to obtain a mode-independent phase reconstruction with the interferometric Hartmann follows the matrix methodology of Hunt.[21] We have M phase-difference sampling points within the pupil, and we have K phase apertures. The individual phases are determined with the following matrix equation:

$$\begin{bmatrix} -1 & -1 & 1 & 1 & 0 & 0 & 0 \ldots 0 \\ 0 & 0 & -1 & -1 & 1 & 1 & 0 \ldots 0 \\ \vdots & \vdots & \vdots & \vdots & \vdots & \vdots & \vdots \; \vdots \; \vdots \\ 1 & -1 & 1 & -1 & 0 & 0 & 0 \ldots 0 \\ 0 & 0 & 1 & -1 & 1 & -1 & 0 \ldots 0 \\ \vdots & \vdots & \vdots & \vdots & \vdots & \vdots & \vdots \; \vdots \; \vdots \end{bmatrix} \begin{bmatrix} \phi_1 \\ \vdots \\ \phi_K \end{bmatrix} = \begin{bmatrix} \Delta\phi x_1 \\ \vdots \\ \Delta\phi x_M \\ \Delta\phi y_1 \\ \vdots \\ \Delta\phi y_M \end{bmatrix}. \tag{10}$$

The arrangement of the row terms is evident from Fig. 2 and Eqs. (1) and (2). Here we have $2M \times K$ terms, and because $K \gg N$, the major disadvantage of this solution is the longer time required to invert the matrix compared with Eq. (9). Once the phases are determined, they can be fit to wave-front polynomials and the residuals used to search for localized phase errors that do not correspond to polynomials.

5. Instrument and Software Design

A. Optomechanical Design

The interferometric Hartmann instrument for the Cassegrain $f/9$ focus has an optical path similar to Fig. 1 and incorporates a doublet collimator and camera (06 LAI 015, Melles-Griot, Irvine, Calif., for both). A Hartmann mask ($d = 380$ μm and $D = 560$ μm, manufactured by Southwestern Laser, Tucson, Ariz.) and blue cutoff filter (RG 715) are placed at the reimaged pupil. The subaperture separation and diameter projected onto the entrance aperture are 170 and 117 mm, respectively. A pierced pickoff mirror provides an acquisition channel with a 1:1 reimager (286 μm/arc sec) so the star image can be monitored as the wave-front corrections are applied. A focal-plane turret allows the selection of the tilted pierced acquisition mirror or a single-mode laser diode reference source (SDL-53-11-G1, Spectra Diode Labs, San Jose, Calif., and LDP-201-06 diode laser power supply, Power Technology, Little Rock, Ark.). The section of the instrument containing the Hartmann mask and focusing lens is replaceable to allow reconfiguration for the other Cassegrain foci of the telescope. Two Apogee KX-260 CCD cameras (Apogee Instruments, Tucson, Ariz.) were selected for use with the instrument (512×512 array of 20-μm pixels). The effective wavelength of the filter and CCD is 820 nm.

An $f/1.25$ to $f/9$ beam converter allows wave-front analysis at the $f/1.25$ prime focus. The intention is for future characterization of the primary mirror figure independent of the secondary, if the need ever arises. A diode laser collimator creates an intermediate pupil that is reimaged back to infinity by an auxiliary doublet. The output beam is compatible with the $f/9$ instrument. Because of the extreme sensitivity of coma to the prime focus position, the instrument is positioned with the high-precision hexapod manufactured by ADS Italia for positioning of the secondary mirror.[15,18] A diode laser and microscope objective provide a reference beam for removal of the instrumental optical aberrations. System interferograms taken with the diode laser reference sources are shown in Fig. 6 for both the $f/9$ and the $f/1.25$ optical paths.

B. Software Design

The software is designed with a scripted graphical user interface written in TCL/TK (tool command language/tool kit widgets) wrapping compiled C routines. The compiled C gives the software computational speed whereas the interpreted graphical user interface provides flexible user control, data flow management, and graphical representation of the results. Because the core calculations are contained in the C code, the analysis software can run independent of the graphical user interface for control automation without user intervention. The software

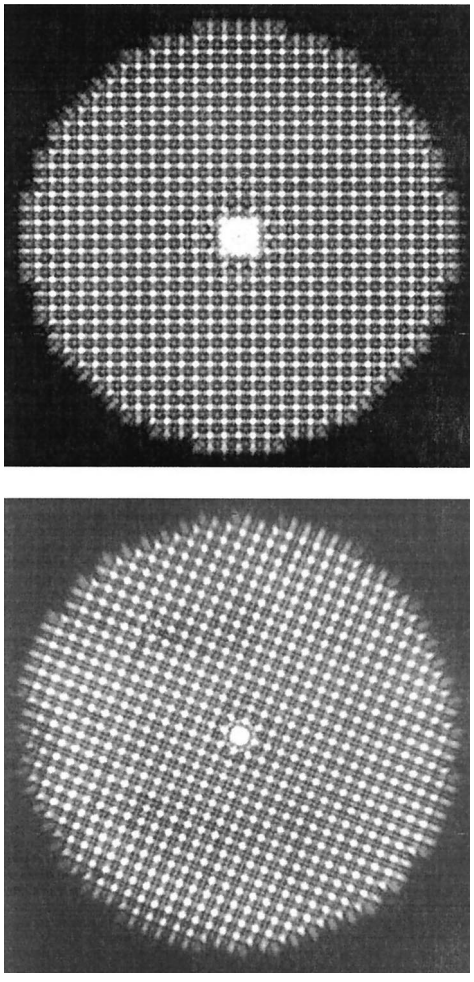

Fig. 6. System interferograms created with a diode laser reference source for the $f/9$ module (top) and the combined $f/1$ and $f/9$ modules.

operates on a Intel computer running Linux. Flexible Image Transport System (FITS) images are collected from the Apogee camera by use of Elwood Downey's CAMERA program (Clear Sky Institute, Inc.).

A mode/phases switch allows the user to select Eq. (9) or (10) for the wave-front error computation. A diffraction point-spread function is calculated from the wave-front errors and both are displayed for the user. Three entry fields fine tune the point-spread function display by allowing the input of the field size, detector defocus, and intensity range. A bar graph of the rms wave-front mode errors is displayed. A gray-scale force map of the correcting primary mirror axial actuator forces is shown as well as the scrolling listbox of force correction values (N) versus the actuator number. More information on the software and instrument is available elsewhere.[22]

6. Primary Mirror Bending and Active Optics Results

A detailed finite-element model is used to determine the influence of each axial support actuator on the primary mirror surface.[23–25] Using these calculations, we converted the wave-front errors into a correcting set of axial forces that are applied to the mirror.[26,27] Figure 7 illustrates the path-length error at a point on a distorted primary mirror surface. The path-length error $d1 + d2$ is just twice the z component of the normal surface error $2N_z$. This relationship allows the observed wave-front phase errors to be related to vector distortions derived from the finite-element calculations.

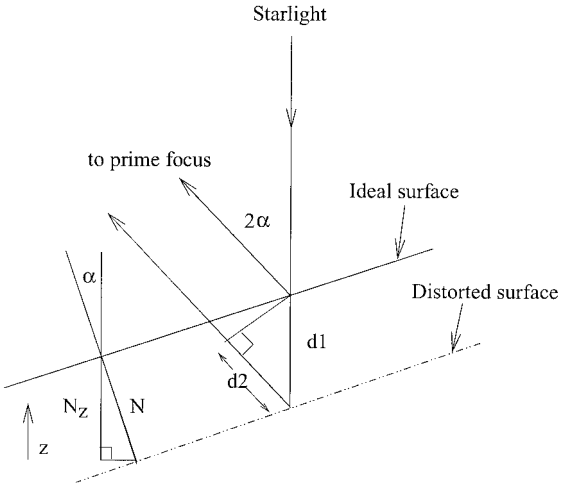

Fig. 7. Exaggerated path-length error of starlight reflecting from a point on a distorted primary mirror showing that $d1 + d2 = 2N_z$. This diagram describes the relationship of the observed wave-front errors to the surface vector displacements derived from the finite-element model calculations of the axial support vector influences on the mirror surface. The angle of the mirror surface normal to the optic axis is α.

A typical interferogram produced by a star through the telescope is shown in Fig. 8 for an integration of 30 s. We calculated the wave-front aberrations by averaging three to five such exposures. When the

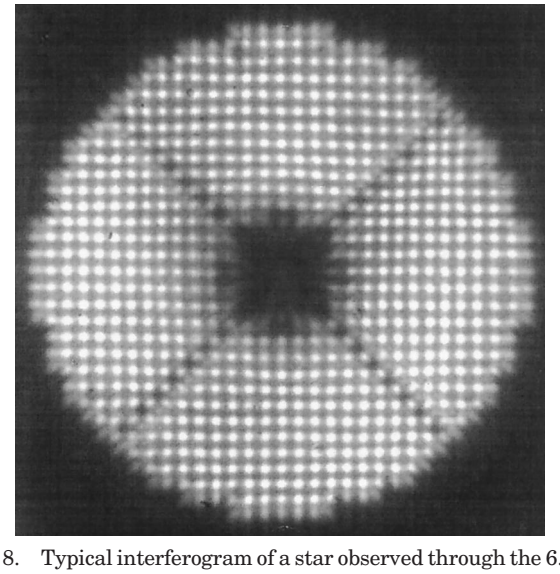

Fig. 8. Typical interferogram of a star observed through the 6.5-m telescope. The shadow and support vanes for the secondary mirror are visible. The phase-difference sensitivity is <70 nm/pixel for this geometry.

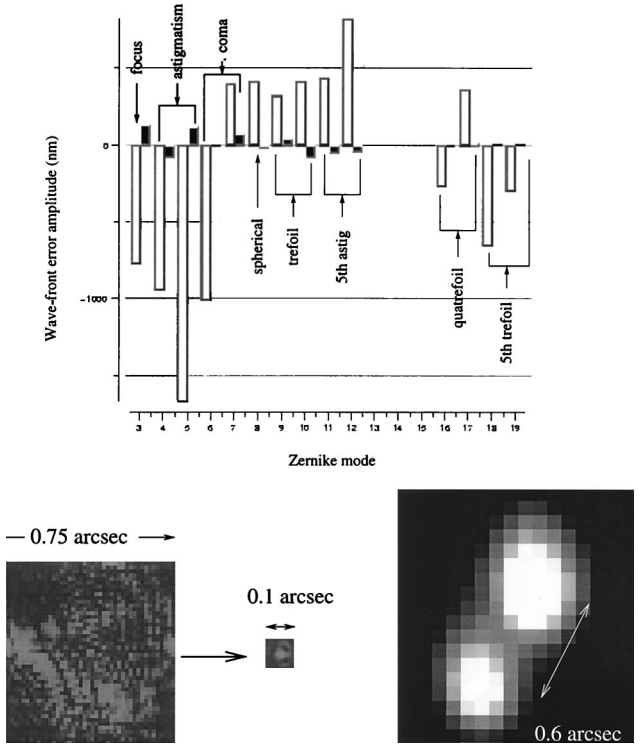

Fig. 9. Wave-front amplitude coefficients (in nanometers) are shown before (white) and after (black) a single correction of primary mirror figure and secondary collimation. The starting aberrations are large because no thermal control of the borosilicate optics has yet been implemented. Fifth-order coma and sixth-order spherical modes (13–15) have not been added to the data reduction yet. The calculated telescope diffraction images before and after the correction are shown in the bottom images. The image of a binary star after the force correction is also shown (0.6-arc sec separation and 0.07-arc sec pixels). The radial profile Gaussian FWHM for each star is 0.35 arc sec including atmospheric seeing and the obvious elongation that is due to an error in the telescope elevation servo.

seeing was less than 0.75 arc sec, wave-front amplitude coefficients as small as 10 nm could be reliably measured. Our results of measuring the wave front, correcting the collimation and primary mirror figure, and then remeasuring the wave-front error are shown Fig. 9. It is important to note that the large starting aberrations are a consequence of the wave front being measured prior to the implementation of the thermal control systems for either the borosilicate primary or the secondary mirrors. However, it does illustrate the useful dynamic range of the Korhonen–Hartmann optical test. After a single force correction, the remaining wave-front error generally grows with decreasing mode number as can be seen in the bar graph of Fig. 9. This is because high-order correction creates spurious low-order bending of the mirror. A second force correction removes most of the remaining error. The diffraction image calculated from the final wave-front error distribution shows that the single force and collimation correction produced an image point-spread function that fits into a 0.1-arc sec box. Also shown is an image of a binary star with 0.6-arc sec separation after the mirror figure and collimation were fully corrected. Each binary component has a Gaussian FWHM of 0.35 arc sec including seeing and the obvious error in elevation tracking.

7. Conclusion

The theory and implementation of an interferometric Hartmann wave-front analyzer for the 6.5-m MMT $f/9$ focus were described. The appeal of the instrument rests in its ability to measure phase differences directly and in the compact interference spots it produces. Because the spot displacement is a large fraction of the spot diameter, small wave-front errors are efficiently detected by the centroiding algorithm. The device has sufficient dynamic range to measure telescope polynomial wave-front amplitudes as small as 10 nm and as large as several micrometers.

Atmospheric seeing places practical limits on the useful subaperture separation in the telescope beam, thus prohibiting the generation of extremely compact interference except under thermally managed laboratory conditions. Compact interference enhances wave-front error sensitivity but requires sparse pupil sampling because the subaperture spacing must be increased. Under conditions of 1-arc sec seeing, a subaperture spacing $>$200 mm washes out the interference, and that is reduced to 100 mm for 2-arc sec seeing. The $f/9$ aperture mask has a subaperture separation of 170 mm, and observations show that interferometric visibility is lost for seeing $>$1.2 arc sec. The median seeing on Mt. Hopkins is 0.7 arc sec.[28]

For a large-aperture telescope, atmospheric phase variations preclude the construction of a high-throughput wave-front sensor with only a few large subapertures optimized to measure only the low-order optical aberrations by use of faint starlight. However, the construction of an efficient wave-front sensor optimized for fine spatial resolution of the telescope beam with bright stars is a practical application of this device and is compatible with atmospheric phase variations.

Images from one- and two-dimensional diffraction modeling illustrate the formation of interference and the detection of phase differences when multiple-wavelength ambiguities are absent. Under these conditions, we presented matrix equations for phase reconstruction and for fitting Zernike gradient monomials using slopes.

A simple modular all-refractive instrument and data analysis software were briefly described for use at the prime and $f/9$ telescope foci. Interferograms from both a reference light source and a telescope beam were shown.

Our first results of using the interferometric Hartmann to optimize mirror figure and collimation show that a single correction iteration is capable of removing large optical aberrations to produce a diffraction image size near 0.1 arc sec (with atmospheric seeing removed). The diffraction limit of the telescope is 0.03 arc sec at an 0.8-μm wavelength. Even without

thermal control of the honeycomb borosilicate optics and when uncorrected telescope drive errors and atmospheric seeing are included, star images of 0.35 arc sec FWHM are obtained.

Observations reported here were obtained at the MMT Observatory, a facility operated jointly by the Smithsonian Institution and the University of Arizona. Tapio Korhonen of Tuorla Observatory in Finland generously answered many questions about designing, using, and implementing the interferometric Hartmann test. Giancarlo Parodi of BCV in Italy and Buddy Martin (Steward Observatory Mirror Laboratory) provided helpful discussions concerning the relationship of the primary mirror finite-element models to the observed wave-front errors. I had several useful discussions with Paul Schecter of the Massachusetts Institute of Technology who developed the Shack–Hartmann wave-front sensors for the Magellan 6.5-m telescopes. Shawn Callahan spearheaded the mechanical design, assembly, and fabrication oversight of the instrument. Don Fisher provided a versatile and powerful image centroiding routine. The MMT Observatory mountain staff and telescope operators provided expert instrument and observing assistance. The MMT Observatory director Craig Foltz allocated operations money for this project. Vatican astronomer Chris Corbally allocated funds for the prototype unit built for the Vatican Advanced Technology Telescope (VATT), and Matt Nelson provided data reduction and observing support at the VATT. Roger Angel first drew my attention to this optical test. The reviewers of this paper provided helpful criticisms of the original draft.

References

1. T. K. Korhonen, "Interferometric method for optical testing and wavefront error sensing," in *Advanced Technology Optical Telescopes II*, L. D. Barr and B. Mack, eds., Proc. SPIE **444,** 249–252 (1984).
2. T. K. Korhonen, S. T. Haarala, J. O. Piironen, and A. K. Sillanpaa, "Interferometric optical test and diffraction based image analysis," in *Advanced Technology Optical Telescopes III*, L. D. Barr, ed., Proc. SPIE **628,** 486–491 (1986).
3. T. K. Korhonen, T. Lappalainen, and A. Sillanpaa, "Hartmann interferometric testing of large mirrors," in *Advanced Optical Manufacturing and Testing II*, V. J. Doherty, ed., Proc. SPIE **1531,** 44–49 (1991).
4. R. N. Wilson, *Reflecting Telescope Optics II* (Springer-Verlag, Berlin, 1999), Sect. 2.3.3.3, pp. 158–161.
5. G. Chanan, M. Troy, F. Dekens, S. Michaels, J. Nelson, T. Mast, and D. Kirkman, "Phasing the mirror segments of the Keck telescopes: the broadband phasing algorithm," Appl. Opt. **37,** 140–155 (1998).
6. G. Chanan, C. Ohara, and M. Troy, "Phasing the mirror segments of the Keck telescopes. II: The narrow-band phasing algorithm," Appl. Opt. **39,** 4706–4714 (2000).
7. H. M. Martin, R. G. Allen, J. H. Burge, L. R. Dettmann, D. A. Ketelsen, W. C. Kittrell, S. M. Miller, and S. C. West, "Fabrication of 6.5 m f/1.25 mirrors for the MMT and Magellan Telescopes," in *Fabrication and Testing of Aspheres*, Vol. 24 of the Trends in Optics and Photonics Series (Optical Society of America, Washington, D.C., 1999), pp. 187–192.
8. S. C. West, S. Callahan, F. H. Chaffee, W. Davison, S. DeRigne, D. Fabricant, C. B. Foltz, J. M. Hill, R. H. Nagel, A. Poyner, and J. T. Williams, "Toward first light for the 6.5-m MMT Telescope," in *Optical Telescopes of Today and Tomorrow*, A. Ardeberg, ed., Proc. SPIE **2871,** 38–48 (1996).
9. J. Antebi, D. O. Dusenbarry, and A. A. Liepins, "Conversion of the MMT to a 6.5-m telescope: the optics support structure and the enclosure," in *Advanced Technology Optical/IR Telescopes VI*, L. M. Stepp, ed., Proc. SPIE **3352,** 513–524 (1998).
10. C. B. Foltz, J. T. Williams, S. C. West, D. G. Fabricant, and H. M. Martin, "The rebirth of the MMT," in *Proceedings of the 16th IEEE Instrumentation and Measurement Technology Conference: Measurements for the New Millennium*, V. Piuri and M. Savino, eds. (Institute of Electrical and Electronics Engineers, New York, 1999), Vol. 2, pp. 633–638.
11. P. M. Gray, S. C. West, and W. Gallieni, "Support and actuation of six secondaries for the 6.5-m MMT and 8.4-m LBT telescopes," in *Optical Telescopes of Today and Tomorrow*, A. Ardeberg, ed., Proc. SPIE **2871,** 374–384 (1996).
12. F. G. Fata and D. G. Fabricant, "Design and support of the 1.7-m f/5 secondary mirror for the MMT conversion," in *Advanced Technology Optical Telescopes V*, L. M. Stepp, ed., Proc. SPIE **2199,** 580–592 (1994).
13. F. Wildi, G. Brusa, A. Riccardi, R. Allen, M. Lloyd-Hart, D. Miller, B. Martin, R. Biasi, and D. Gallieni, "Progress of the MMT adaptive optics program," in *Adaptive Optics Systems and Technology II*, R. K. Tyson, D. Bonaccini, and M. C. Roggemann, eds., SPIE **4494,** 11–18 (2001).
14. P. M. Gray, J. M. Hill, W. B. Davison, S. Callahan, and J. T. Williams, "Support of large borosilicate honeycomb mirrors," in *Advanced Technology Optical Telescopes V*, L. M. Stepp, ed., Proc. SPIE **2199,** 691–702 (1994).
15. W. Gallieni and R. Pozzi, "Secondary mirrors support M2/f15 and M2/f9 hexapod design," Tech. Rep. 31 (Multiple Mirror Telescope Observatory, Tucson, Ariz., 1997).
16. D. Gallieni, "M2/f15 and M2/f9 hexapod data package," Tech. Rep. 34 (Multiple Mirror Telescope Observatory, Tucson, Ariz., 1998).
17. D. Gallieni, "Secondary mirrors support: M2/F5 hexapod design technical report," Tech. Rep. 36 (Multiple Mirror Telescope Observatory, Tucson, Ariz., 2001).
18. S. C. West, D. Fisher, P. Spencer, and T. Trebisky, "6.5m MMT f/9-f/15 hexapod laboratory calibration," Conversion Tech. Memo 00-3 (Multiple Mirror Telescope Observatory, Tucson, Ariz., 2000), http://nemo.as.arizona.edu/~swest/pdfs/f9hexcalib.pdf.
19. D. L. Fried, "Statistics of a geometric representation of wavefront distortion," J. Opt. Soc. Am. **55,** 1427–1435 (1965).
20. H. M. Martin, "Image motion as a measure of seeing quality," Publ. Astron. Soc. Pac. **99,** 1360–1370 (1987).
21. B. R. Hunt, "Matrix formulation of the reconstruction of phase values from phase differences," J. Opt. Soc. Am. **69,** 393–399 (1979).
22. S. C. West, S. Callahan, and D. Fisher, "An interferometric-Hartmann wavefront analyzer for the 6.5m MMT, and the first results for collimation and figure correction," Tech. Rep. 37 (Multiple Mirror Telescope Observatory, Tucson, Ariz., 2001), http://nemo.as.arizona.edu/~swest/pdfs/ih_sh.pdf.
23. BCV progetti, "MMT conversion project: mirror 6.5m F/1.25: finite element model," Rep 8, Rev. 0 (BCV progetti, Milano Italy, 1994).
24. BCV progetti, "MMT conversion project: mirror 6.5m F/1.25: axial and lateral support optimisation," Rep. 7, Rev. 0 (BCV progetti, Milano Italy, 1994).
25. BCV progetti, "MMT conversion project: MMT 6.5m F/1.25: axial supports influence functions," Rep. 6, Rev. 0 (BCV progetti, Milano Italy, 1995).

26. H. M. Martin, S. P. Callahan, B. Cuerden, W. B. Davison, S. T. DeRigne, L. R. Dettmann, G. Parodi, T. J. Trebisky, S. C. West, and J. T. Williams, "Active supports and force optimization for the MMT primary mirror," in *Advanced Technology Optical/IR Telescopes VI*, L. M. Stepp, ed., Proc. SPIE **3352,** 412–423 (1998).
27. S. C. West and H. M. Martin, "Correcting 6.5m primary mirror figure errors with the active supports," Conversion Tech. Memo 00-2 (Multiple Mirror Telescope, Tucson, Ariz., 2000), http://nemo.as.arizona/~swest/pdfs/figureCorrectionsMemo.pdf.
28. C. B. Foltz, "Seeing improvements resulting from improved chamber ventilation," Conversion Tech. Memo 96-4 (Multiple Mirror Telescope Observatory, Tucson, Ariz., 1996).